Solvent-Driven Gate Opening in MOF-76-Ce: Effect on CO2 Adsorption

Ethiraj, Jayashree; Bonino, Francesca; Vitillo, Jenny G.; Lomachenko, Kirill A.; Lamberti, Carlo; Reinsch, Helge; Lillerud, Karl Petter; Bordiga, Silvia. Solvent-Driven Gate Opening in MOF-76-Ce: Effect on CO2 Adsorption. CHEMSUSCHEM. 9 (7) pp: 713-719.
DOI: 10.1002/cssc.201501574

Solvent driven gate opening in MOF-76-Ce: effect on CO_2 adsorption.

Jayashree Ethiraj,[1] Francesca Bonino,*[1] Jenny G. Vitillo,[1,2] Kirill A. Lomachenko,[1,3] Carlo Lamberti,[1,3] Helge Reinsch,[4] Karl Petter Lillerud[4] and Silvia Bordiga[1]

[1] Department of Chemistry, NIS and INSTM Reference Centre, University of Turin, Via G. Quarello 15, I-10135 and Via P. Giuria 7, I-10125, Turin, Italy

[2] Dipartimento di Scienza ed Alta Tecnologia, Università degli Studi dell'Insubria, Via Lucini 3, I-22100-Como, Italy

[3] Southern Federal University, Zorge street 5, 344090 Rostov-on-Don, Russia

[4] inGAP centre of Research-based Innovation, Department of Chemistry, University of Oslo, SemSælandsvei 26, N-0315 Oslo, Norway

Abstract

A cerium based metal-organic framework with MOF-76 topology has been synthesized by a very simple and fast solvo-thermal method that has been tested for 1 g yield. Variable Temperature-powder X-Ray Diffraction and X-ray absorption data, analyzed by Rietveld and multiple-scattering EXAFS methods, revealed high thermal stability and the presence of three different stable structures. XANES and FTIR spectroscopies probed the presence of Ce(III) characterized by coordinatively unsaturated sites that however do not play the major role in CO_2 adsorption. The material revealed excellent CO_2 adsorption properties: the highest gravimetric capacity of 15 wt% is observed at 1.1 bar in the case of the sample activated at 250°C in vacuum, while the strongest interaction energy of 35 kJ/mol is observed in the case of the sample activated at 150°C. The negligible nitrogen uptake of the sample activated at 150°C indicates this material as a promising candidate for N_2/CO_2 separation purposes.

Introduction

Microporous MOFs based on lanthanide metal ions or clusters represent a group of porous materials which possesses interesting coordination, electronic, and optical properties.[1] Porous isostructural lanthanide-based MOFs, having the composition [Ln(BTC)(H_2O)·4.3H_2O] or Ln–BTC (Ln: Ce, Tb, and Y; BTC: 1,3,5-benzenetricarboxylate), and exhibiting a tetragonal structure were synthesized by ultrasonic irradiation at room temperature and their luminescence properties were studied.[2]

The Y-based MOF Y(BTC)(H_2O)•4.3H_2O, showed permanent porosity, selective gas adsorption and good H_2 capacity upon activation.[3]

Gustasfsson et al.[1c] developed a family of homeotypic porous lanthanide MOFs [Ln(BTC)(H_2O)] • (H_2O, DMF) with various metal ions (Nd, Sm, Eu, Gd, Tb, Ho, Er, and Yb). The structure was first described as coincident with MOF-76 for Tb(BTC)(H_2O)1.5(DMF).[4] The structures of the as-synthesized compounds were tetragonal with 1D channels, showing accessible lanthanide ions and exhibited high thermal stability.

By focusing attention on Ce metal ions, Ce-based Werner-type tetrahedra were employed for size selective luminescent detection of natural carbohydrates via incorporation of amide groups.[5] Li et al.[6] succeeded in obtaining single crystals of a Ce based BTC MOF in order to get a well-defined 3D structure but the synthetic procedure showed difficulties in producing the material at gram-scale. Furthermore, a very recent paper[7] reported that Ce-BTC structure collapses after removal of the solvent guest molecules.

In the present work, a very simple and rapid one-pot solvo-thermal procedure is reported for the synthesis of MOF-76-Ce material. This method allows easy up scaling of the material. In respect to previous published data, the material revealed an improved thermal stability (up to 450°C) and the appearance of new well-defined structures upon heating. The intermediate (partly desolvated structure) showed selective adsorption towards CO_2 over N_2 and then it is here proposed for CO_2/N_2 separation purposes, while the fully desolvated one is characterized by one of the highest CO_2

volumetric density.[8] As successfully applied to other MOFs systems,[9] the combination of several structural and spectroscopic techniques have been used to disclose the complex structure of MOF-76-Ce.

Results and discussion

Structure evolution of MOF-76-Ce

MOF-76-Ce was synthesized as described in the Experimental section. Details on morphology, thermal stability and vibrational features are reported as Supporting Information (Sections S1-S3). In-situ Variable Temperature Powder XRD (VT-PXRD) data of MOF-76-Ce (formula: $[Ce(BTC)]H_2O_nDMF_m$) collected in N_2 flow, in the 25-600°C temperature range, are reported in Figure 1. Three distinct structural modifications are refined from the PXRD data. Starting from the "*as made*" sample (**MOF-76-Ce-fs, fully solvated**), the most relevant changes are observed at 180°C (**MOF-76-Ce-hs, half solvated**) with a further evolution that ends at 350°C (**MOF-76-Ce-ds, desolvated**). In the 250-300°C range, the patterns do not change substantially while, starting from 325°C the 100, 010 reflection shift slightly towards higher angles: this is caused by the chains of Ce-atoms moving slightly closer when the flexibility of the BTC linkers increases with temperature. The connectivity of the structure is unchanged during the structural changes. The transformations were found to be due to removal of water and DMF molecules from the channels in the $[Ce(BTC)]\cdot H_2O_nDMF_m$ structure. Similar features have been reported on single crystals of lanthanide MOFs with seven-coordinated Ln(III) ions linked by BTCs.[1c] At 575°C there is a complete structure collapse with formation of CeO_2 and coke in agreement with the weight loss seen in TGA analysis (section S2 in Supporting Information).

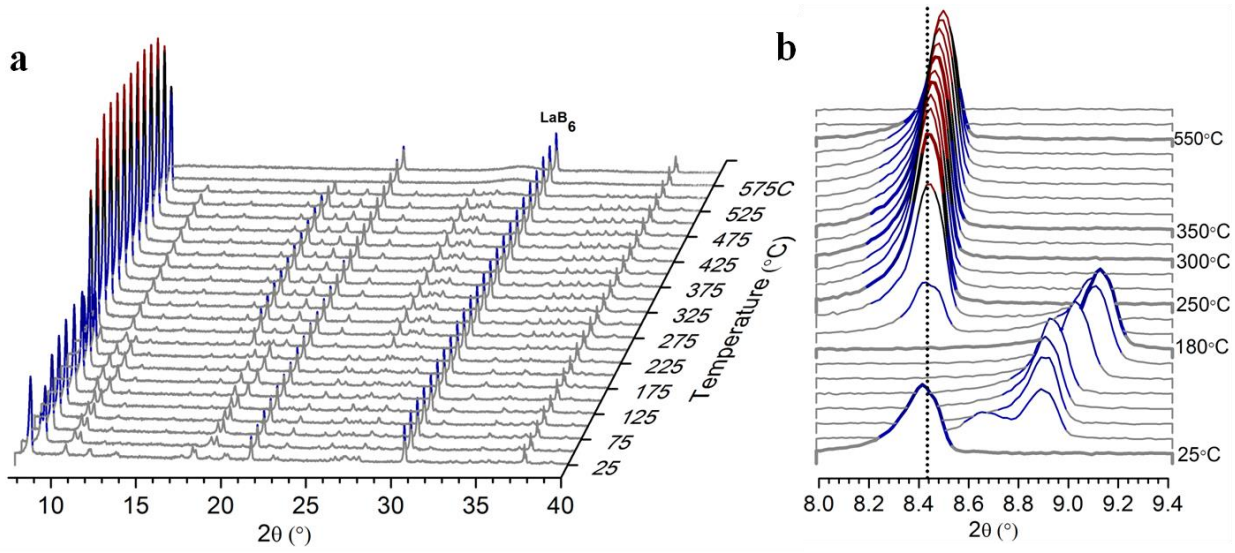

Figure 1. VT-PXRD in N_2 flow showing structural changes of MOF-76-Ce during thermal treatment**. a,** PXRD patterns collected in the 25-600°C temperature range (λ = 1.5418 Å). LaB_6 is used as internal standard (reflection at 30.39°). **b,** Zoom on the low angle reflections.

Rietveld refinement of the structures was carried out using high resolution powder patterns recorded in N_2 flow at the temperatures for which the three structures were identified: 25, 180 and 350°C. Experimental patterns and refinement results are reported in Supporting Information S4 (see Figure S4 and Table S1), while graphical representation of the structures obtained is illustrated in Figure 2. The pattern measured at 25°C showed very strong similarities with a simulated pattern of MOF-76.[1c, 4] Indeed, the Rietveld refinement confirmed that this compound is a Ce-based analogue of the MOF-76-structure. The final structures reported in Figure 2 have been obtained after several iterated PXRD and Ce L_3 edge EXAFS refinements. First, the structure obtained as a result of initial PXRD refinement was used as a model for EXAFS fitting. Then, the best-fit local environment of Ce atoms obtained by EXAFS was implemented into the periodic model of the whole material and the PXRD refinement was run again. Resulting structure was subsequently subjected to the new EXAFS fitting procedure and so on, until after several iterations the convergence of structural parameters was reached.[9]

The inorganic building unit is based on distorted pentagonal CeO_7-bipyramids. In these polyhedra, six oxygen atoms are part of carboxylate groups while one oxygen atom belongs to a solvent molecule, water or DMF (see Figure 2 left panel and Figure 3, **MOF-76-Ce-fs**). Each BTC linker is connected to six Ce-atoms, two in one cerium chain and four on the opposite chain. Each carboxylate group bridges two Ce-atoms. The orientation of the BTC linkers alternates, forming regular wriggled (sinusoidal) chains of Ce atom (see Figure 2 left panel). The sheets are connected in a similar way with another set of BTC linkers orthogonal to the plane of the picture. This wriggling in and out of the plane in two directions arranges the CeO_7-units into helical chains forming a 4_3-screw axes. The organic trimesate anions (BTC linkers) are situated in parallel with the (100) and (010) planes, forming non-interconnected square-shaped channels. In the fully solvated structure, the channels are lined with four coordinated solvent molecules, while in the half solvated (180^{o}C) structure, the solvent molecules are removed in an ordered manner (Figure 2, medium panel, **MOF-76-Ce-hs**). Solvent molecules distribution reported in Figure 2 are arbitrarily represented. In particular in case of fully solvated sample, alternate arrangements of water and DMF have been considered. For the sake of simplicity disordered un-bonded solvent molecules have been omitted. In case of **MOF-76-Ce-hs** structure (Figure 2, medium panel), in principle DMF and water should be both taken into account, however only DMF molecules fit perfectly (while water would be too small) and distort the channels and thereby the structure by a diagonal contraction of the channels. In this intermediate structure, the solvent molecules are removed at two opposite corners of the channels, which lead to a distortion of the angle at these corners from ideal 90° in **MOF-76-Ce-fs** to 68° in **MOF-76-Ce-hs**. As a consequence, the opposite angles are expanded from 90° to 112°. Rhombic channels are therefore observed in which the coordinated solvent molecules are present as non-connecting pillars pointing into the pores. Please note that partially desolvated structure (**MOF-76-Ce-hs**) shows the major changes into the free space topology: in fact channels along [001] direction are strongly bent (middle structure, bottom row of Figure 2) and the DMF

molecules are much more protruding into the channels than in case of **MOF-76-Ce-fs** (left structure, bottom row of Figure 2). When all solvents molecules are removed, the structure relaxes to a square shape similar to the one with symmetric loading of solvent molecules. (Figure 2, right panel**, MOF-76-Ce-ds**). In this framework all coordinated solvent molecules are removed and the original symmetry is restored. The connectivity of the Ce-ions, involving the carboxylate groups remains unchanged. Ce-ions simply changes the local symmetry from a distorted pentagonal bipyramid in **MOF-76-Ce-fs** to a distorted trigonal prism in **MOF-76-Ce-ds**.

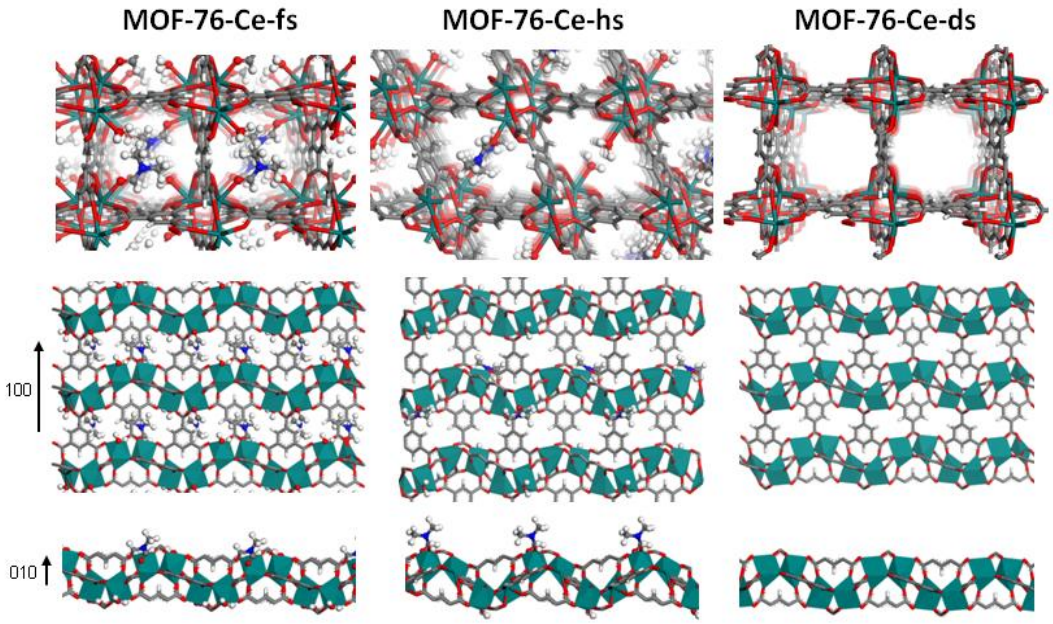

Figure 2. Structures of MOF-76-Ce. Left panel: **MOF-76-Ce-fs;** central panel: **MOF-76-Ce-hs**; right panel: **MOF-76-Ce-ds.** Top row: tridimensional representation (view along the 001 direction) of the frameworks with sticks (solvent molecules are represented by sticks and balls). Cerium - dark cyan; oxygen - red; nitrogen - blue; carbon - grey, hydrogen - white. Middle row: layers of Ce and BTC linkers viewed along the 010 direction; Bottom row: one chain of Ce with the coordinating carboxylic groups and solvent molecules (viewed along the 100 direction). In case of **MOF-76-Ce-fs** and **MOF-76-Ce-hs**, DMF and water have been arbitrarily alternated into the framework. For **MOF-76-Ce-fs**, solvent molecules not coordinated to Ce sites have been omitted. Coordinative structure at Cerium sites is evidenced with polyhedra in medium and bottom rows.

MOF-76-Ce-hs and **MOF-76-Ce-ds** PXRD patterns were reproduced upon activation in vacuum at 150°C and at 250°C (see Figure S5 in Supporting Information), showing that both structures are obtained in slightly different conditions when samples are treated in vacuum or in flow respectively. Activated samples lose crystallinity if re-exposed to air.

As announced, in order to refine the local coordination environment of cerium, Ce L_3-edge EXAFS spectra were measured *in situ* during the activation. The data were collected for **MOF-76-Ce-fs**, during heating up to 350°C in He flow, and after subsequent cooling back to room temperature without interrupting the flow of He (**MOF-76-Ce-ds**). In this way, the **MOF-76-Ce-fs** and **MOF-76-Ce-ds** bond distances were directly comparable without bias due to thermal effects.

Figure 3a shows the experimental EXAFS signals for initial and final states of the activation process. The data indicate that the major changes upon activation happen in the nearest environment of Ce atoms (oxygen and carbon atoms within 3.5 Å from Ce that contribute to the phase-uncorrected EXAFS in the range of 1.5-3.0 Å), since the largest peak centered at 2 Å gets dramatically perturbed, while farther-away coordination shells are much less affected. The main changes upon activation happen around 90°C and they were monitored by the mass spectrometer (see Figure S6b), which indicates that they coincide with the release of water. However, only the loss of one water molecule per cerium atom is certainly not sufficient to cause such a remarkable change in the EXAFS signal. At the same time, the loss of a larger fraction of coordinated first shell ligands would not have been consistent with the crystal structure, indicated by PXRD. In order to explain the changes in the spectra, the EXAFS data were fitted, using the corresponding PXRD geometries as starting points. Figure 3b shows the cluster used for **MOF-76-Ce-fs**. The activated structure lacks solvent oxygen O_{sol}, but otherwise is qualitatively similar and therefore is not presented for the sake of brevity. Obtained fits are in good agreement with experimental data (Figure 3c, d). In **MOF-76-Ce-fs**, the main peak is due to the scattering from four pairs of oxygen atoms (O1-4), one pair of carbons (C1) and one oxygen of an adsorbed solvent molecule (O_{sol}).

Despite the impressive decrease in the intensity of the first EXAFS peak in the activated material, it was confirmed that, upon activation until 350°C, only the solvent molecule desorbs, while all other atoms in the nearest vicinity of Ce remain. The decrease of the main peak is explained by a severe antiphase effect due to the significant elongation of Ce–O3 distance from 2.55 Å to 2.75 Å. While in solvated material the contribution from this path (dark-green curve in Figure 3c,d) is almost perfectly in phase with those of O1 and O2, in the activated form it goes exactly out of phase which, accompanied by the loss of solvent oxygen O_{sol}, causes the observed damping effect. Consequently, the contribution from C1 and O4 becomes visible as a separate peak around 2.6 Å, whereas in the solvated material it is only a shoulder on the high-R side of the main maximum. (see details in Supporting Information, Table S2 and Table S3).

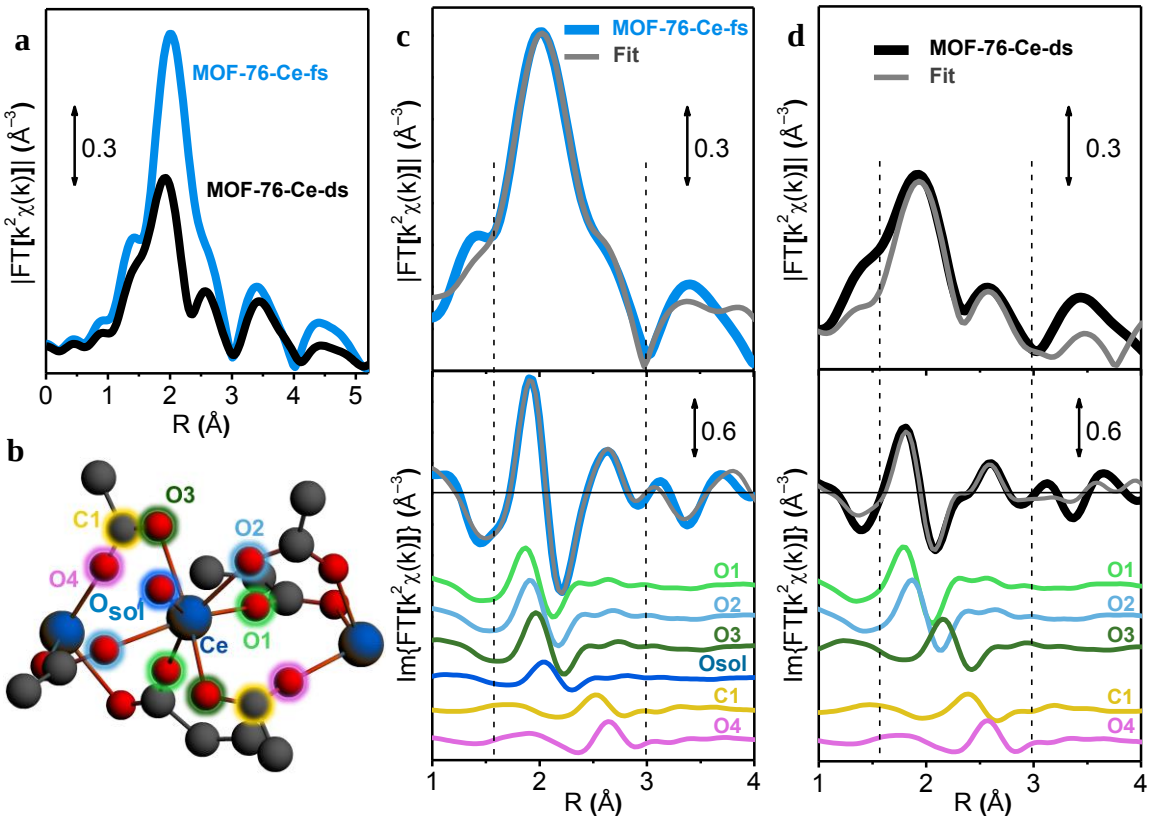

Figure 3. EXAFS analysis of MOF-76-Ce. **a,** Fourier-transform (FT) modulus of experimental phase-uncorrected k^2-weighted Ce L_3-edge EXAFS signal of **MOF-76-Ce**. **b,** Atomic cluster used for EXAFS fitting. Colour code: blue – Ce, red – O, grey – C. Atoms that constitute the nearest

coordination of Ce and contribute the most to the EXAFS signal are labelled and highlighted by coloured halos. Absorbing Ce atom is in the center of the cluster. **c-d,** Comparison between experimental and fitted EXAFS signals for **MOF-76-Ce-fs** (c) and **MOF-76-Ce-ds** (d) sample. Top panels show the moduli of EXAFS FT, while the bottom panels exhibit the imaginary parts of the FT together with the contributions of the principal scattering paths. Vertical dashed lines indicate the boundaries of the fitted region. The colour of each path's signal matches the colour of the halo in the panel (b) assigned to the atoms that form the path. With exception of solvent oxygen O_{sol}, each path is formed by the two atoms equidistant from Ce that have the halos of the same colour.

The oxidation state of Ce ion in **MOF-76-Ce** was studied by XANES and FT-IR methods (see Figure 4).

Ce L_3-edge XANES spectra serve as a very reliable indicator for Ce oxidation state, since the shapes of the L_3 edge for Ce (IV) and Ce (III) are completely different. While Ce (IV) gives rise to a double-peaked main maximum with two low-energy shoulders, Ce (III) produces a very intense single-peaked white line.[10] Typical examples that illustrate these two different cases are cerium (IV) oxide and cerium (III) nitrate, which were used in our XANES experiment as reference compounds (Figure 4a). Ce L_3-edge XANES spectra were simultaneously collected with EXAFS data showing no substantial change of the Ce oxidation state, along the sample treatment in inert flow.

Trivalent Ce species, with at least one coordination vacancy, were monitored in **MOF-76-Ce-ds** upon CO adsorption followed by IR spectroscopy (Figure 4b). It is well-known that the CO vibrational frequency is able to shift differently after coordination by Ce^{3+} or Ce^{4+} centers.[11] In this experiment, 10 mbar of CO were dosed at liquid nitrogen temperature on a self-supported pellet of **MOF-76-Ce-ds** (obtained by pretreating in dynamic vacuo at 250°C for 2h). The pressure in the cell was gradually reduced by contemporaneous recording of spectra. Three distinct contributions

appeared at 2155, 2149 and 2137 cm^{-1}. The band at 2137 cm^{-1}, being the first one to be removed upon lowering the pressure, was assigned to physisorbed CO condensed in the pores. The doublet at higher frequencies (2155 and 2149 cm^{-1}) required more prolonged pumping to disappear and, for this reason, they can be assigned to CO interacting with acidic sites. At higher coverage, the feature at 2155 cm^{-1} was dominant, while the one at 2149 cm^{-1} was only a shoulder. By decreasing CO pressure, the feature at 2155 cm^{-1} disappears more rapidly than the one at 2149 cm^{-1}. As CO vibrational mode on MOF open metal sites is intermediate between metals in oxides and metals grafted in different systems,[12] the doublet can be ascribed to adsorption on Ce^{3+} sites, as bands due to Ce^{4+} were expected at frequencies higher than 2156 cm^{-1},[11] in agreement with XANES results (Figure 4a). The hypothesis of two different Ce^{3+} sites, characterized by different strength and abundancy, was ruled out being not supported by the structure. Thus, the band at 2155 cm^{-1} could be tentatively assigned to CO interacting with one Ce^{3+} site and the band at 2149 cm^{-1} to CO bridged on two close Ce^{3+} sites, on the basis of literature reports.[13]

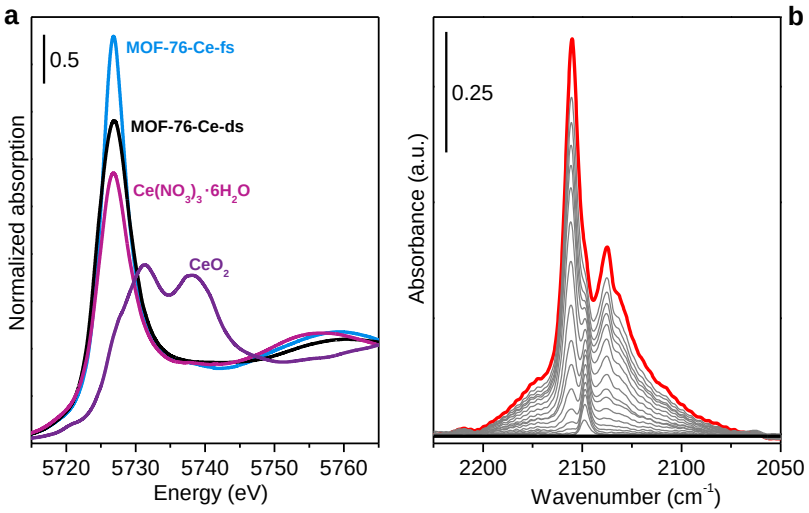

Figure 4. **a**, Ce L_3-edge XANES spectra of MOF in **MOF-76-Ce-fs** and **MOF-76-Ce-ds**, compared to Ce (IV) oxide and Ce (III) nitrate hexahydrate. All the spectra have been collected at room temperature. **b**, FTIR spectra of CO adsorption at -196°C recorded on **MOF-76-Ce-ds** (black

curve); red and gray curves represent respectively the highest (p=10 mbar) and the intermediate coverages obtained upon progressive outgassing.

CO_2 and N_2 adsorption on MOF-76-Ce

Adsorption properties towards CO_2 of **MOF-76-Ce-hs** and **MOF-76-Ce-ds** were also explored. All the presented data indicate that the two materials, in spite of their similar structural features, such as the first coordination sphere of Ce sites, are expected to behave substantially differently.

Volumetric CO_2 isotherms recorded at 25°C in the 0-1.1 bar pressure range on **MOF-76-Ce-hs** and **MOF-76-Ce-ds** are reported in Figure 5a for both adsorption and desorption branches (full and open circles, respectively). **MOF-76-Ce-hs** and **MOF-76-Ce-ds** show comparable uptake up to the pressure of 0.15 bar, while at higher pressure (1.1 bar) **MOF-76-Ce-ds** reveals the higher CO_2 storage capacity of 4 mol/kg (15 wt%).

Table 1 reports CO_2 storage capacity in the case of the two samples together with the corresponding BET and Langmuir surface areas calculated from N_2 adsorption at -196°C (see Supporting Information S8 for further details). The Langmuir surface area value measured for **MOF-76-Ce-ds** is quite high (999 m^2/g), whereas for **MOF-76-Ce-hs** this value was not measurable, indicating that the pore of the material are not accessible to N_2. Moreover, a negligible external surface area was expected from the large dimension of the MOF crystals (> 10 μm, see Figure S1). "Channels gates" are not open for N_2 as they are for CO_2 in case of **MOF-76-Ce-hs**: it is thus evident that **MOF-76-Ce-hs** is expected to be a suitable material for N_2/CO_2 separation purposes, whereas **MOF-76-Ce-ds** would be preferable for CO_2 storage. Nitrogen measurements were then repeated at 25°C, in order to quantify the selectivity of these materials in CO_2/N_2 flows. The N_2 isotherms are reported in Figure 5a (triangles) whereas the adsorption selectivities (defined as $S_{CO_2/N_2} = \frac{n_{CO_2} p_{N_2}}{n_{N_2} p_{CO_2}}$, where p are the partial pressures of the gas and n is the gas adsorbed at p on the material in the

corresponding pure gas isotherm) for a 15% CO_2 / 85% N_2 flow at 25°C and 1 bar are reported in Table 1. These values confirmed what expected indicating for **MOF-76-Ce-hs** large selectivities.[8g] It is interesting that a partial desolvation of the MOF structure, besides lowering the CO_2 adsorption capacities as expected, causes an increase in the selectivity of the material. It could be then suggested the utility to retest the best performing microporous structures reported so far in the literature for CO_2/N_2 separation at different desolvation degree.

In case of **MOF-76-Ce-ds**, although the CO_2 adsorbed amounts are halved with respect to the ones reported for the MOF with best performances in these adsorption conditions (Mg-MOF-74, 21.6 wt%),[8g] the high affinity of this material toward CO_2 can be qualitatively estimated by normalizing the CO_2 uptake to the material surface area (see Figure 5b). This graph suggests that MOFs with open metal sites (as HKUST-1, Mg-MOF-74 and Ni-MOF-74) adsorb, at pressures ≤ 1 bar, more CO_2 than the others, because of the positive effect of the cations on the storage capacity (e.g **MOF-76-Ce-ds** has very similar performance to Mg-MOF-74)[8g]. Moreover, when CO_2 volumetric density (often considered a more crucial parameter for implementation of a material in a CO_2 sequestration plant than gravimetric density)[8h] is considered, **MOF-76-Ce-ds** at 25°C and 1 bar shows a value of 145 cm^3 STP cm^{-3}. This makes **MOF-76-Ce-ds** the third best performing MOF from this point of view and with a value close to the ones reported for Mg-MOF-74 (174 cm^3 STP cm^{-3}),[8h] UTSA-16 (162 cm^3 STP cm^{-3})[8h] and NaX (177 cm^3 STP cm^{-3}).

Table 1. Surface areas, CO_2 storage capacity (at 1.1 bar and 25°C) and differential heat of adsorption of CO_2 (q_{diff}, at 25°C and 0.002 bar) on MOF-76-Ce. Adsorption selectivities for a gas mixture 15% CO_2 / 85% N_2 at atmospheric conditions are also reported (S_{CO_2/N_2}).

	S_{BET} (m^2/g)	$S_{Langmuir}$ (m^2/g)	CO_2 amount (mol/kg)	CO_2 storage wt%	S_{CO_2/N_2}	q_{diff} (kJ/mol)
MOF-76-Ce-hs	n.p.*	n.p.*	1.1	4.6	33.8	35

MOF-76-Ce-ds	754	999	4.0	15	15.4	21

*n.p.: not porous

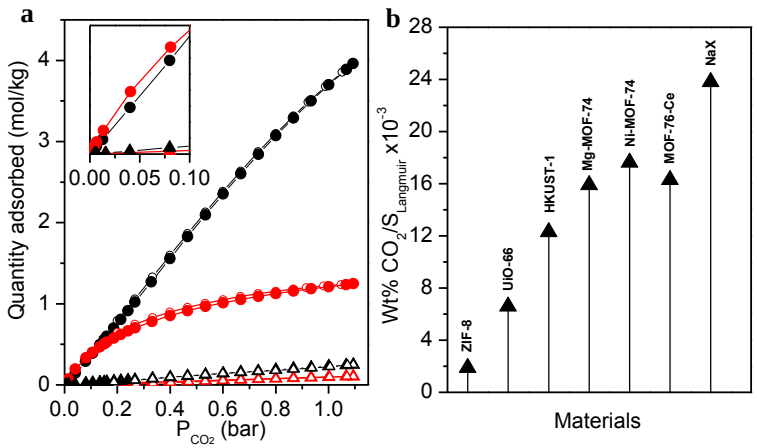

Figure 5. N_2 and CO_2 Volumetric Isotherms. **a**, Excess CO_2 and N_2 adsorption and desorption isotherms at 25°C obtained on **MOF-76-Ce-hs** (red full and open circles respectively in case of CO_2, while for N_2 triangles were adopted) and **MOF-76-Ce-ds** (black full and open circles respectively in case of CO_2, while for N_2 triangles were adopted). **b**, Comparison of CO_2 adsorption capacities normalized to the material surface area (in m^2/g) as measured at 25°C and 1 bar for **MOF-76-Ce-ds,** other MOFs[8g] and NaX.

More complex and intriguing is the explanation of CO_2 adsorption profile on **MOF-76-Ce-hs**, as this material has a very small accessible volume (as testified by the impossibility of measuring any surface area by N_2 adsorption at -196°C).

For the sake of completeness, CO_2 volumetric measurements were performed also on **MOF-76-Ce-ds** activated at 350°C and 450°C (see Supporting Information S9).

The CO_2 affinity to **MOF-76-Ce-hs** and **MOF-76-Ce-ds** was further investigated by means of FTIR and microcalorimetric measurements. FTIR adsorption study indicates that CO_2 asymmetric stretching mode is only slightly perturbed, also in the case of fully desolvated sample (see Supporting Information S10), not allowing to evidence any difference between the two materials.

Concerning microcalorimetry, CO_2 adsoprtion was measured in the pressure range of 0-0.1 bar at 30°C: the results are summarized in Figure 6. The isotherms are reported in Figure 6a and they clearly demonstrate a Henry-type adsorption because of the low pressure considered (only 1/10 of the Ce atoms are involved). In the very first stages of the adsorption, the amount of CO_2 measured reaches the value of 0.3 mmol/g for **MOF-76-Ce-hs**: this is considerably higher than for **MOF-76-Ce-ds**. The same trend is observed in the volumetric isotherms reported in the inset of Figure 5a. Furthermore, the calorimetric data show a large difference in the initial heat of adsorption (Q^{int} J/g) for the two materials: the value obtained for **MOF-76-Ce-hs** is 2.5 times the value obtained for **MOF-76-Ce-hs** (Figure 6b). At the lowest pressure, the differential adsorption heat (Figure 6c) for **MOF-76-Ce-hs** is nearly 35 kJ/mol, a value that is close to the value obtained on other well-known MOFs with open metal site like HKUST-1 (29 kJ/mol)[8f] and Mg-MOF-74 (39-47 kJ/mol).[8d, 8e] The heat of adsorption decreases till to reach a plateau at 28 kJ/mol. Surprisingly, **MOF-76-Ce-ds** shows from the beginning a lower interaction energy of 21 kJ/mol that is quite stable in the full range of the experimental data. This difference, both in values and in evolution during the increasing coverages, can be justified by the different nature of CO_2 interaction towards the surface sites. In case of **MOF-76-Ce-hs**, the significantly higher interaction energy of CO_2 could be due to the fact that the CO_2 molecule has the right size to be entrapped inside the small cavities generated by the persistence of DMF molecules (see Figure 2 medium panel) while, in case of in **MOF-76-Ce-ds,** the interaction is due to end-on Ce(III)···CO_2 adducts formed in presence of a coordination vacancy at cerium sites. Calorimetric measurements were also carried out on the material activated in vacuum at 350°C, confirming the similar behavior obtained in case of **MOF-76-Ce-ds** (see Figure S10 in Supporting Information).

Both microcalorimetric and volumetric data show the reversibility of CO_2 adsorption at 30°C and 25°C.

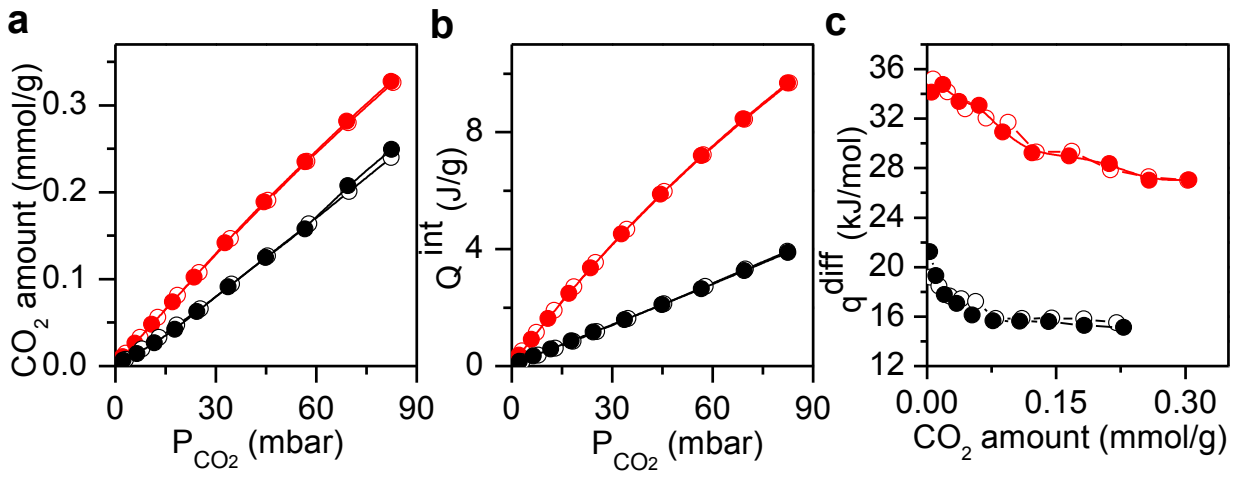

Figure 6. CO_2 Microcalorimetric data. **a**, Volumetric CO_2 isotherms. **b**, Calorimetric isotherms. **c**, Differential heat distributions obtained on **MOF-76-Ce-hs** (red) and **MOF-76-Ce-ds** (black). Empty and full squares indicates the primary and secondary isotherms obtained at each temperature of activation.

Conclusions

A fast one pot solvo-thermal synthesis for **MOF-76-Ce,** a material with a very high thermal stability, has been optimized. Three different structures were recognized by means of VT-XRD technique. Their structures are characterized by a different ratio of solvent molecules to Ce ions (1:1, 1:2 and zero). Cerium has 3+ oxidation state and exhibits one coordination vacancy per metal center when the MOF is fully activated.

Volumetric CO_2 adsorption isotherms showed the highest value of 15 wt% at 1.1 bar for the sample activated at 250°C. However, microcalorimetry revealed, in the lowest pressure range, the strongest interaction energy of 35 kJ/mol for the sample activated at 150°C. The material activated at 150°C is not accessible to N_2, while CO_2 is strongly bonded at 30°C. This observation could become of extreme relevance in developing this material for post combustion CO_2 capture, also thanks to its easy synthetic procedure.

Cyclability of **MOF-76-Ce** upon multiple adsorption-desorption cycles will be investigated in future works.

Experimental Section

MOF-76-Ce (as synthetized composition: $[Ce(BTC)]H_2O_nDMF_m$) was synthesized using an exact amount of trimesic acid (H_3BTC 95%, Sigma Aldrich, 0.525 g, 2.5 mmol) dissolved in a solvent mixture of N,N-dimethylformamide (Sigma Aldrich, anhydrous DMF, 99.8%, 100 ml) and millipore distilled water (50 ml). Then an exact amount of $Ce(NO_3)_3 \cdot 6H_2O$ (Sigma Aldrich, 99.99%, 2.171g, 5 mmol) was added to the mixture, that was stirred for 15 min and placed in a 250 ml DrySyn heating block set at 140ºC for 30 min. The precipitate was filtered, dried at 50ºC for 2h and washed with 30ml DMF. The final yield was of 1 g.

Powder X-ray Diffraction PXRD patterns have been collected with a X'Pert PRO MPD diffractometer from PANalytical working in Bragg-Brentano geometry, using as source a ceramic tube with a Cu anode. Scattered photons have been collected by a X'celerator detector equipped with Ni filter to attenuate K_β. Non-ambient chamber Anton Paar XRK900 with Be windows was used to collect the XRPD patterns as a function of the temperature, in N_2 flow (flow rate 20 ml/min). The temperature program was set in order to measure the sample each 25°C and waiting at each step 25 min before to collect the diffractogram. The sample has been heated with a heating rate equal to 2°C/min. The measured temperature of the experimental chamber is subject to an error within 5°C. The sample was mixed with 20% wt% of LaB_6 (NIST 660a standard) as reference for both peak position and sample stage height.

High Resolution Powder X-ray Diffraction (HR-PXRD) data were collected on a Bruker D8 Advance with LynxEye XE detector in capillary transmission mode. The radiation was CuK-alpha-1 selected by a Ge (111) monochromator. The sample was packed in an open 0.5 mm internal diameter quartz capillary between plugs of quartz wool and mounted in a Norby flow cell [14] and

heated with a Leister LE mini hot air blower. The experiment was carried out under a constant flow of nitrogen (10 ml/min, 99.99%, AGA). An initial structure change occurred when N_2 flow was applied at 25°C. The sample was heated to 180°C at a rate of 2°C/min with rapid data collections. The sample was then held at 180°C and a series of patterns were collected with a count time of 1 s/step and step size of 0.014°, until the structure was stabilized. The sample was then heated to 350°C at the same rate. A pattern was collected at 350°C always with a count time of 1 s/step and step size 0.014°.

All processing of the PXRD data was carried out with TOPAS. The structural transformation for the intermediate was carried out with PowderCell and force-field calculations were performed with Materials Studio using the Universal Force Field (UFF).

X-ray absorption spectra at Ce L_3-edge (5723 eV) were collected at the BM23 beamline of the European Synchrotron Radiation Facility (ESRF). The storage ring current was between 150 and 200 mA. Incident radiation was subject to harmonic rejection by Si mirror and monochromatized by a double-crystal Si (111) monochromator. The data were acquired up to the Ce L_2-edge (6164 eV) that limited the EXAFS signal down to k≈10 $Å^{-1}$. Acquisition step was set to 0.3 eV in the near-edge region and $\Delta k = 0.035$ $Å^{-1}$ in the EXAFS part of the spectrum. We used three He/N_2-filled ionization chambers as I_0, I_1 and I_2 detectors, placing chromium foil between I_1 and I_2 for energy calibration. Acquisition time was set to 1 s/point in the XANES region and then increased quadratically up to 2 s/point in the end of the spectrum. XANES and EXAFS data were analysed using Demeter 0.9.20 package [15]. Sample treatment was carried out in *in situ* cell, flowing 80 ml of helium per minute. During the activation, the sample was heated up to 350°C with a ramp rate of 4°C per minute and then cooled down to 30°C.

FT-IR spectra were collected on a Nicolet-6700 spectrometer equipped with a MCT B type detector, in the range of 4000-400 cm^{-1}, in transmission mode with a 2 cm^{-1} resolution, and averaged on 64 scans.

N_2 and CO_2 adsorption isotherms were collected at 25°C on a volumetric instrument (Micromeritics ASAP 2020 sorption analyzer) by use of an isothermal water bath at 25°C.

N_2 adsorption isotherms were also collected at -196°C for surface area evaluations.

Before each volumetric measurement, the samples (> 200 mg) were activated under vacuum at 150, 250, 350 and 450^oC respectively on the same vacuum equipment used for the FT-IR measurements. The samples were transferred in the measurement cell in a MBraun Star glove box (H_2O, O_2 < 0.5 ppm).

The heat of adsorption and the adsorption isotherms were measured simultaneously by means of a C80 microcalorimeter (Calvet type, Setaram, France) at 30°C (a well-established stepwise procedure is described in Supporting Information and Ref. [[16]]). Before each calorimetric measurement, the samples were activated under vacuum at different temperatures. After the first adsorption run, the samples were outgassed at 30°C overnight in the calorimeter before the second adsorption run was performed, such that the non-desorbable (irreversible) adsorbed fraction could be determined.

Acknowledgements

MIUR-PRIN 2010-2011 (project n:2010A2FSS9) is kindly acknowledged for the financial support. KAL and CL acknowledge the funding from the Mega-grant of the Russian Federation Government to support scientific research at SFedU, no. 14.Y26.31.0001. We acknowledge the use of the Norwegian national infrastructure for X-ray diffraction and scattering (RECX), Norwegian

Research Council project 208896. Cesare Atzori, master thesis student, is kindly acknowledged for his help in performing some of the experiments. Dr. Alberto Castellero and Dr. Gianluca Fiore are acknowledged for the help in VT-XRD measurements.

Supporting Information

Scanning Electron Microscopy; Thermogravimetric analysis; Raman Spectroscopy; High Resolution Powder X-ray Diffraction and Rietveld refinement; Comparison of PXRD of MOF-76-Ce treated in vacuum and in flow; N_2 adsorption isotherms; EXAFS: evolution of local environment of Ce species upon activation; EXAFS: fitting details; In situ FT-IR Spectroscopy of CO_2 adsorption; Volumetric CO_2 isotherms; Calorimetric CO_2 isotherms.

Keywords: Adsorption, Cerium, Carbon Dioxide Capture, Metal-Organic Frameworks, X-ray Diffraction

References

[1] a) Y. Chen, S. Q. Ma, *Rev. Inorg. Chem.* **2012**, *32*, 81-100; b) L. D'Arras, C. Sassoye, L. Rozes, C. Sanchez, J. Marrot, S. Marree, C. Aymonier, *New J. Chem.* **2014**, *38*, 1477-1483; c) M. Gustafsson, A. Bartoszewicz, B. Martin-Matute, J. L. Sun, J. Grins, T. Zhao, Z. Y. Li, G. S. Zhu, X. D. Zou, *Chem. Mater.* **2010**, *22*, 3316-3322.

[2] N. A. Khan, M. M. Haque, S. H. Jhung, *Eur. J. Inorg. Chem.* **2010**, 4975-4981.

[3] J. H. Luo, H. W. Xu, Y. Liu, Y. S. Zhao, L. L. Daemen, C. Brown, T. V. Timofeeva, S. Q. Ma, H. C. Zhou, *J. Am. Chem. Soc.* **2008**, *130*, 9626-9627.

[4] N. L. Rosi, J. Kim, M. Eddaoudi, B. L. Chen, M. O'Keeffe, O. M. Yaghi, *J. Am. Chem. Soc.* **2005**, *127*, 1504-1518.

[5] Y. Liu, X. Wu, C. He, Y. Jiao, C. Y. Duan, *Chem. Commun.* **2009**, 7554-7556.

[6] Z. Li, K. Liu, *Acta Cryst.* **2011**, *E67*, m1020.

[7] M. Almáši, V. Zeleňáka, M. Opanasenkob, I. Císařovác, *Catal. Today* **2015**, *243*, 184-194.

[8] a) Z. Zhang, Z.-Z. Yao, S. Xiang, B. Chen, *Energy Environ. Sci.* **2014**, *7*, 2868-2899; b) O. Shekhah, Y. Belmabkhout, Z. Chen, V. Guillerm, A. Cairns, K. Adil, M. Eddaoudi, *Nat. Commun.* **2014**, *5*; c) P. Nugent, Y. Belmabkhout, S. D. Burd, A. J. Cairns, R. Luebke, K. Forrest, T. Pham, S. Ma, B. Space, L. Wojtas, M. Eddaoudi, M. J. Zaworotko, *Nature* **2013**, *495*, 80-84; d) D. Britt, H. Furukawa, B. Wang, T. G. Glover, O. M. Yaghi, *Proc. Natl. Acad. Sci. U. S. A.* **2009**, *106*, 20637-20640; e) S. R. Caskey, A. G. Wong-Foy, A. J. Matzger, *J. Am. Chem. Soc.* **2008**, *130*, 10870-10871; f) L. Grajciar, A. D. Wiersum, P. L.

Llewellyn, J. S. Chang, P. Nachtigall, *J. Phys. Chem. C* **2011**, *115*, 17925-17933; g) K. Sumida, D. L. Rogow, J. A. Mason, T. M. McDonald, E. D. Bloch, Z. R. Herm, T.-H. Bae, J. R. Long, *Chem. Rev.* **2012**, *112*, 724-781; h) S. C. Xiang, Y. B. He, Z. J. Zhang, H. Wu, W. Zhou, R. Krishna, B. L. Chen, *Nat. Commun.* **2012**, *3*, 954; i) J. G. Vitillo, *RSC Adv.* **2015**, *5*, 36192-36239.

[9] a) L. Valenzano, B. Civalleri, S. Chavan, S. Bordiga, M. H. Nilsen, S. Jakobsen, K. P. Lillerud, C. Lamberti, *Chem. Mater.* **2011**, *23*, 1700-1718; b) S. Bordiga, F. Bonino, K. P. Lillerud, C. Lamberti, *Chem. Soc. Rev.* **2010**, *39*, 4885-4927; c) J. H. Cavka, S. Jakobsen, U. Olsbye, N. Guillou, C. Lamberti, S. Bordiga, K. P. Lillerud, *J. Am. Chem. Soc.* **2008**, *130*, 13850-13851; d) F. Bonino, S. Chavan, J. G. Vitillo, E. Groppo, G. Agostini, C. Lamberti, P. D. C. Dietzel, C. Prestipino, S. Bordiga, *Chem. Mater.* **2008**, *20*, 4957-4968; e) J. Hafizovic, M. Bjorgen, U. Olsbye, P. D. C. Dietzel, S. Bordiga, C. Prestipino, C. Lamberti, K. P. Lillerud, *J. Am. Chem. Soc.* **2007**, *129*, 3612-3620; f) C. Prestipino, L. Regli, J. G. Vitillo, F. Bonino, A. Damin, C. Lamberti, A. Zecchina, P. L. Solari, K. O. Kongshaug, S. Bordiga, *Chem. Mater.* **2006**, *18*, 1337-1346.

[10] a) L. Barrio, G. Zhou, I. D. Gonzalez, M. Estrella, J. Hanson, J. A. Rodriguez, R. M. Navarro, J. L. G. Fierro, *Phys. Chem. Chem. Phys.* **2012**, *14*, 2192-2202; b) J. Elfallah, S. Boujana, H. Dexpert, A. Kiennemann, J. Majerus, O. Touret, F. Villain, F. Lenormand, *J. Phys. Chem.* **1994**, *98*, 5522-5533; c) G. Jacobs, P. M. Patterson, L. Williams, E. Chenu, D. Sparks, G. Thomas, B. H. Davis, *Appl. Catal. A-Gen.* **2004**, *262*, 177-187; d) S. H. Overbury, D. R. Huntley, D. R. Mullins, G. N. Glavee, *Catal. Lett.* **1998**, *51*, 133-138; e) A. V. Soldatov, T. S. Ivanchenko, S. Della Longa, A. Kotani, Y. Iwamoto, A. Bianconi, *Phys. Rev. B* **1994**, *50*, 5074-5080.

[11] a) F. Vindigni, M. Manzoli, T. Tabakova, V. Idakiev, F. Boccuzzi, A. Chiorino, *Phys. Chem. Chem. Phys.* **2013**, *15*, 13400-13408; b) C. Binet, M. Daturi, J. C. Lavalley, *Catal. Today* **1999**, *50*, 207-225.

[12] a) S. Chavan, F. Bonino, J. G. Vitillo, E. Groppo, C. Lamberti, P. D. C. Dietzel, A. Zecchina, S. Bordiga, *Phys. Chem. Chem. Phys.* **2009**, *11*, 9811-9822; b) S. Bordiga, L. Regli, F. Bonino, E. Groppo, C. Lamberti, B. Xiao, P. S. Wheatley, R. E. Morris, A. Zecchina, *Phys. Chem. Chem. Phys.* **2007**, *9*, 2676-2685.

[13] E. Garrone, R. Bulanek, K. Frolich, C. O. Arean, M. R. Delgado, G. T. Palomino, D. Nachtigallova, P. Nachtigall, *J. Phys. Chem. B* **2006**, *110*, 22542-22550.

[14] P. Norby, *Mater. Sci. Forum* **1996**, *228-231*, 147-152.

[15] B. Ravel, M. Newville, *J. Synchrot. Radiat.* **2005**, *12*, 537-541.

[16] V. Bolis, in *Calorimetry and Thermal Methods in Catalysis, Vol. 154* (Ed.: A. Auroux), Springer, Heidelberg **2013**, pp. 3-50.

Table of Contents

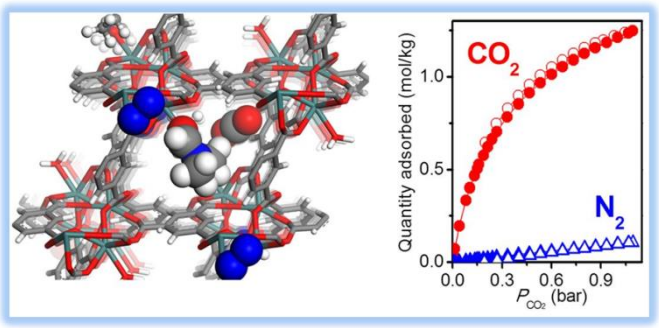

A fast one pot solvo-thermal synthesis for **MOF-76-Ce,** a material with a very high thermal stability, has been optimized. **MOF-76-Ce** showed three different structures with high potentiality in CO_2 capture, being the highest value of 15 wt% at 1.1 bar for the sample activated at 250°C.